

Interatomic Coulombic decay widths of helium trimer: Ab initio calculations

Přemysl Kolorenč and Nicolas Sisourat

Citation: The Journal of Chemical Physics 143, 224310 (2015); doi: 10.1063/1.4936897

View online: http://dx.doi.org/10.1063/1.4936897

View Table of Contents: http://scitation.aip.org/content/aip/journal/jcp/143/22?ver=pdfcov

Published by the AIP Publishing

Articles you may be interested in

Ab initio lifetimes in the interatomic Coulombic decay of neon clusters computed with propagators J. Chem. Phys. **126**, 164110 (2007); 10.1063/1.2723117

Calculation of interatomic decay widths of vacancy states delocalized due to inversion symmetry J. Chem. Phys. **125**, 094107 (2006); 10.1063/1.2244567

Ab initio investigation of the autoionization process Ar * (4 s P 2 3 , P 0 3) + Hg \rightarrow (Ar – Hg) + + e $\overline{}$: Potential energy curves and autoionization widths, ionization cross sections, and electron energy spectra J. Chem. Phys. **122**, 184309 (2005); 10.1063/1.1891666

The effect of intermolecular interactions on the electric properties of helium and argon. I. Ab initio calculation of the interaction induced polarizability and hyperpolarizability in He 2 and Ar 2

J. Chem. Phys. 111, 10099 (1999); 10.1063/1.480361

An accurate potential energy curve for helium based on ab initio calculations

J. Chem. Phys. 107, 914 (1997); 10.1063/1.474444





Interatomic Coulombic decay widths of helium trimer: Ab initio calculations

Přemysl Kolorenč^{1,a)} and Nicolas Sisourat^{2,3}

¹Charles University in Prague, Faculty of Mathematics and Physics, Institute of Theoretical Physics, V Holešovičkách 2, 180 00 Prague, Czech Republic

²Sorbonne Universités, UPMC Univ Paris 06, UMR 7614, Laboratoire de Chimie Physique Matière et Rayonnement, F-75005 Paris, France

³CNRS, UMR 7614, Laboratoire de Chimie Physique Matière et Rayonnement, F-75005 Paris, France

(Received 8 September 2015; accepted 19 November 2015; published online 9 December 2015)

We report on an extensive study of interatomic Coulombic decay (ICD) widths in helium trimer computed using a fully *ab initio* method based on the Fano theory of resonances. Algebraic diagrammatic construction for one-particle Green's function is utilized for the solution of the many-electron problem. An advanced and universal approach to partitioning of the configuration space into discrete states and continuum subspaces is described and employed. Total decay widths are presented for all ICD-active states of the trimer characterized by one-site ionization and additional excitation of an electron into the second shell. Selected partial decay widths are analyzed in detail, showing how three-body effects can qualitatively change the character of certain relaxation transitions. Previously unreported type of three-electron decay processes is identified in one class of the metastable states. © 2015 AIP Publishing LLC. [http://dx.doi.org/10.1063/1.4936897]

I. INTRODUCTION

Despite their apparent simplicities, small helium clusters are peculiar quantum objects. The low helium atomic mass and the very weak interaction potential between the atoms lead to their extreme delocalization. As a result, the mean average interatomic distance in the helium dimer attains an enormous value of about 52 Å. Larger clusters (trimers, tetramers, . . .), while being much less extended than the dimer, also exhibit remarkable interatomic distance distributions. ²

This unusual physical property allows the investigation of interatomic electronic processes over a wide range of distances and geometries. In this context, the helium dimer has been used in a series of work³⁻⁸ to investigate the interatomic Coulombic decay (ICD). 9-12 ICD is an ultrafast non-radiative decay process of excited atoms or molecules embedded in a chemical environment. For example, after simultaneous ionization and excitation of one helium atom in a cluster, this excited ion relaxes via ICD by transferring its excess energy to a neighboring atom which is thus ionized. In helium dimer, measured spectra show that ICD takes place for interatomic separation up to 14 Å, implying that the two atoms can efficiently exchange energy over more than 45 times their atomic radius.³ For still larger interatomic distances, ICD becomes too slow and is quenched by local radiative decay of the initial excitation.

No less striking features are observed also in the helium trimer. The pair distribution function of ${}^4\text{He}_3$ extends from 3.3 to 12 Å (full width at half maximum) and the mean interatomic distance is predicted to be around 10.4 Å for ${}^4\text{He}_3$ and even 20.5 Å for ${}^3\text{He}{}^4\text{He}_2$. 13,14 The width of this distribution stems from the delocalized nature of a single (ground) vibrational state. It should be mentioned that the helium trimer has a

Computing the observable energy distributions of the decay products involves treating the nuclear dynamics of the system during and after the decay process. Relevant decay widths of the involved metastable states in the configuration space spanned during the dynamics are an essential input for such simulations. Therefore, in the present work we study the ICD widths of the helium trimer subjected to simultaneous ionization and excitation (into the L-shell) of one helium atom,

$$He^{+}(1s^{0}2p^{1}) + He(1s^{2}) + He(1s^{2})$$

 $\longrightarrow He^{+}(1s^{1}) + He^{+}(1s^{1}) + He(1s^{2}).$

We have computed fully *ab initio* the total and partial decay widths of the corresponding ionization satellite states (ionized states in which the vacancy is accompanied by an excitation of an electron from an occupied to virtual orbital) for different geometries, focusing mainly on the isosceles configuration.

single excited state which is an Efimov state with a size about 10 times larger than the ground state. This long predicted state has been recently observed, 15 but its influence on the observed pair distribution in helium trimer has been ruled out by the experiment.¹³ Furthermore, the extreme delocalization causes that no preferential geometry of the trimer can be determined. 13,16 Knowledge of relevant quantities such as potential energy surfaces and total and partial decay widths over a wide range of geometries and interatomic distances is therefore necessary for a full understanding and modeling of ICD in the helium trimer. The experimental observables are the kinetic energy distribution of the ions and of the secondary electron. Both observables reflect strongly the geometrical distribution of the neutral system and the total and partial decay widths.^{3,5} Owing to the recent remarkable developments in coincidence spectroscopy techniques, the trimer thus provides an unique opportunity to investigate the geometrical dependence of the ICD widths.

a) Electronic mail: kolorenc@mbox.troja.mff.cuni.cz

The partial decay widths for different channels exhibit diverse dependence on the interatomic distances. In the region of large interatomic separations, the asymptotic behavior of the widths can be analyzed in terms of the virtual photon transfer mechanism. We show that three-body effects play an important role and qualitatively change the dependence of the ICD widths compared to straightforward expectations based on the results obtained for the helium dimer.⁶

Larger number of neighboring atoms also opens new decay channels which have no equivalent counterparts in dimers and can be accessible only by rather exotic pathways. In the present study, an example is provided by a new type of electron transfer mediated decay (ETMD), which involves three actively participating electrons. In normal two-electron ETMD¹⁷ process, a neighboring atom donates an electron to fill the initial vacancy on the ion while the released energy is simultaneously transferred either to the donor [ETMD(2)] or to another neighbor [ETMD(3)], leading to a secondary electron being ejected to continuum. Therefore, the ETMD channels are distinguished by the initially ionized species being neutral in the final state. In the helium trimer, the ETMD transition is further accompanied by simultaneous local recombination of the excited electron back to the 1s orbital on the initially ionized-excited atom.

The outline of the article is the following: in Sec. II we review the Fano-algebraic diagrammatic construction (ADC)-Stieltjes method and describe its novel modification used to calculate the ICD widths (Sec. II C). In Secs. III A and III B, the geometrical dependence of the ICD widths in helium trimer is reported and discussed. The asymptotic behavior of the widths is then explained in the framework of the virtual photon mechanism in Sec. III C. The article is concluded in Sec. IV. Atomic units $(e = \hbar = m_e = 1)$ are used in the presented equations.

II. THE METHOD

The decay widths presented in this work were calculated using the Fano-ADC-Stieltjes method. 18-20 It is an ab initio \mathcal{L}^2 method which relies on Fano-Feshbach theory of resonances²¹⁻²³ and algebraic diagrammatic construction in the intermediate states representation [ISR-ADC]²⁴ for the many-electron wave functions. Stieltjes imaging technique²⁵ is used for the normalization and interpolation of the discretized continuum. The method was described in detail in the references cited above, but since in the present work we apply an original approach to partitioning of the configuration space into the bound states and continuum subspaces, we will review it here in order to provide the necessary context. The decay widths are calculated in the fixed-nuclei approximation with the nuclear coordinates entering only as parameters. Therefore, the wave functions considered below represent only the electronic part of the system.

A. Fano theory of resonances

In the theory of resonances developed by Fano²¹ and—in a convenient projection-operator formalism—by Feshbach,²²

the wave function Ψ_E at an energy E near a resonance is represented as a superposition of \mathcal{L}^2 discrete (Φ) and continuum $(\chi_{\beta,\epsilon})$ components

$$\Psi_{E,\alpha} = a_{\alpha}(E)\Phi + \sum_{\beta=1}^{N_c} \int C_{\beta,\alpha}(E,\epsilon) \chi_{\beta,\epsilon} d\epsilon, \qquad (1)$$

where the index $\alpha=1,\ldots,N_c$ numbers the independent solutions of the Schrödinger equation. In the projection-operator formalism, this decomposition is realized by partitioning of the Hilbert space into the continuum subspace $\mathcal P$ and the subspace $\mathcal Q$ which contains the bound-like discrete states. The discrete states and continuum states can be interpreted as the initial and final states of the relaxation process, respectively. In the specific case of ICD in clusters, the bound-like component Φ corresponds to the singly ionized state, typically created by an inner-valence ionization of one of the cluster subunits (or, in the case of helium clusters studied in the present paper, by simultaneous ionization and excitation of a single atom). It is characterized by its mean energy

$$E_{\Phi} = \langle \Phi | \hat{H} | \Phi \rangle, \tag{2}$$

 \hat{H} being the full electronic Hamiltonian of the system. The N_c decay channels in Eq. (1) are defined by the energetically accessible doubly ionized states of the cluster with energies $E_{\beta} < E$. Integration runs over the energy ϵ of the outgoing electron. The continuum functions $\chi_{\beta,\epsilon}$ (in the context of scattering theory they are often referred to as the background continuum) are assumed to diagonalize the Hamiltonian to a good approximation,

$$\langle \chi_{\beta',\epsilon'} | \hat{H} - E | \chi_{\beta,\epsilon} \rangle \approx (E_{\beta} + \epsilon - E) \delta_{\beta',\beta} \times \delta(E_{\beta'} + \epsilon' - E_{\beta} - \epsilon).$$
 (3)

Analytic expression for the decay width can then be derived,

$$\Gamma = \sum_{\beta=1}^{N_c} \Gamma_{\beta} = 2\pi \sum_{\beta=1}^{N_c} |\langle \Phi | \hat{H} - E_r | \chi_{\beta, \epsilon_{\beta}} \rangle|^2, \tag{4}$$

where E_r is the real energy of the decaying state (resonance), $E_r \approx E_\Phi$, and ϵ_β is the asymptotic kinetic energy of the ejected electron for the decay channel β , such that $E_\beta + \epsilon_\beta = E_r$. Note that the total decay width has the form of a sum of partial decay widths Γ_β for the individual channels which determine their relative intensity. For more detailed discussion of the application of the Fano theory to the Auger decay see also Ref. 26.

B. Algebraic diagrammatic construction

To evaluate formula (4), approximations for the initial (Φ) and final state $(\chi_{\beta,\epsilon})$ wave functions have to be provided. In the present case, they correspond to either singly ionized N-electron cluster or doubly ionized cluster plus an electron in continuum, i.e., to (N-1) electron states (the first electron ejected during the initial ionization step is neglected in the Fano theory). Such states can be conveniently constructed using the single-ionization ADC technique. It has been originally developed within the Green's function formalism.²⁷

Later, the ADC methodology was reformulated in the more lucid intermediate state representation,²⁴ which will be briefly reviewed here.

Consider perturbation-theoretically corrected ("correlated") ground state of the neutral *N*-electron system,

$$\Psi_0^N = \Phi_0^N + \Psi_0^{(1)} + \Psi_0^{(2)} + \Psi_0^{(3)} + \cdots, \tag{5}$$

where Φ_0^N is the Hartree-Fock (HF) ground state determinant and $\Psi_0^{(n)}$ is *n*th perturbative wave function correction. A complete orthonormal set of the (N-1)-electron basis functions $\tilde{\Psi}_J$ (intermediate states) can be obtained by the following procedure. First, *correlated excited states* are constructed by applying the so-called physical excitation operators

$$\{\hat{C}_{J}\} \equiv \{c_{i}; c_{a}^{\dagger}c_{i}c_{j}, i < j; c_{a}^{\dagger}c_{b}^{\dagger}c_{i}c_{j}c_{k}, a < b, i < j < k; \ldots\}$$
(6)

to neutral ground state (5),

$$\Psi_J^0 = \hat{C}_J \Psi_0^N. \tag{7}$$

Here, c_i and c_a^{\dagger} are annihilation and creation operators, respectively, with the subscripts i,j,k,\ldots relating to the occupied and subscripts a,b,c,\ldots to unoccupied (virtual) spin-orbitals. The capital index J numbers individual configurations while in square brackets ([J]) it denotes the whole excitation classes. These can be classified as one-hole (1h, [J] = 1), two-hole-one-particle (2h1p, [J] = 2), and so on. Unlike the case of the familiar configuration interaction (CI) expansion, in which the excitation operators C_J are applied directly to the HF ground state, the correlated excited states Ψ_J^0 are not orthogonal. The basis of intermediate states (ISs) is obtained by orthonormalizing them in two steps. First, Gram-Schmidt orthogonalization between the excitation classes is performed to obtain the precursor states,

$$\Psi_J^{\#} = \Psi_J^0 - \sum_{\substack{K \\ [K] < [J]}} \langle \tilde{\Psi}_K | \Psi_J^0 \rangle \tilde{\Psi}_K, \tag{8}$$

i.e., the states belonging to the higher excitation class are orthogonalized to those of all the lower excitation classes. Second, the orthonormal ISs are obtained by symmetrical orthogonalization of the precursor states *within each excitation class*,

$$\tilde{\Psi}_{J} = \sum_{\substack{J'\\|J'|=|J|}} \left(\underline{\underline{\rho}}^{\#-(1/2)}\right)_{J'J} \Psi_{J'}^{\#}, \tag{9}$$

where $\left(\underbrace{\rho^{\#}}_{J'J} \right) = \langle \Psi_{J'}^{\#} | \Psi_{J'}^{\#} \rangle$ is the overlap matrix of the precursor states belonging to the same excitation class. Note that the ISs of the lower classes [K] < [J], appearing in Eq. (8), are available when needed for orthogonalization of the class [J] if the procedure is applied iteratively.

Any state of the (N-1)-electron system can be represented in the basis of ISs,

$$\Psi_q^{(N-1)} = \sum_{i} \sum_{|J|=i} Y_{q,J} \tilde{\Psi}_J. \tag{10}$$

Consistent truncation of the perturbation series for ground state (5) at a specific order n and of expansion (10) at

the appropriate class [J] yields nth order ADC scheme, abbreviated ADC(n). Specifically, ADC(2) scheme for singly ionized states describes the many-electron wave functions in the basis of 1h and 2h1p ISs. In the corresponding Hamiltonian matrix, the coupling between 1h states is treated in the second order while that between 1h and 2h1p states is evaluated in the first order in Coulomb interaction. In the extended second order scheme [ADC(2)x], used in the present work, the first order couplings between 2h1p states are also taken into account. Detailed description of the single ionization ADC(2) and ADC(3) schemes can be found in Ref. 28. The major advantages of using ADC instead of CI scheme are faster convergence and size extensivity of the resulting expansions, at the cost of a more complicated evaluation of the Hamiltonian matrix.

C. Combining ADC with the Fano theory: universal Q– \mathcal{P} partitioning scheme

To utilize the ADC expansion for the Fano theory and evaluation of decay width (4), the key step is to perform the partitioning of the space spanned by the ISs (configuration space) into the continuum subspace $\mathcal P$ of the final states of the decay and the complementary subspace $\mathcal Q$, containing the discrete components. The initial metastable state is then represented by a discrete state Φ selected among the eigenstates of the ADC Hamiltonian in the $\mathcal Q$ subspace while the decay continuum $(\chi_{\beta,\epsilon})$ is approximated by all the eigenstates χ_i of the ADC Hamiltonian in the $\mathcal P$ subspace.

In rigorous theory, the fundamental difference between the two subspaces is that \mathcal{P} corresponds to states with at least one electron in continuum while Q contains only states represented by square-integrable wave functions. In practical applications, however, this distinction is lost as quantum-chemical calculations are routinely carried out in Gaussian basis sets, hence even the continuum is represented by \mathcal{L}^2 wave functions. Therefore, other criteria of the classification of ISs have to be devised. In the present problem, both initial and final states are of the 2h1p character—cluster with two vacancies and one electron either in virtual orbital or in continuum. It is thus this class of ISs within which the $Q-\mathcal{P}$ separation has to be performed.

The major obstacle is that there is in general no direct one-to-one correspondence between the square integrable ISs of 2h1p character and physical states of doubly ionized cluster plus one electron in continuum. Previously, two partitioning schemes have been developed, both with a rather limited range of application: (i) in the case of ICD in heteronuclear dimers with molecular orbitals (MO) localized on specific atoms, the classification can be readily done utilizing the observation that the final states of the interatomic decay processes such as ICD are distinguished by the two vacancies being localized on different constituents of the system; ¹⁸ (ii) in homonuclear dimers with MOs delocalized due to the inversion symmetry, the following localization procedure can be used to adapt the ISs to the calculation of the interatomic decay widths. ¹⁹ First, specific couples of 2h1p ISs characterized by the same particle orbital and hole orbitals forming gerade-ungerade pairs are selected. Then, the respective 2×2 sub-blocks of the ADC

Hamiltonian matrix are diagonalized. It can be shown that the lower-energy eigenstates correspond to two-site 2h1p states with holes localized on different atoms while the higher-energy ones to the one-site states with both holes localized on a single atom. This construction therefore leads to ISs adapted to the calculation of interatomic decay widths. Indeed, the two-site states belong to the subspace $\mathcal P$ of final states and the one-site states contribute solely to the $\mathcal Q$ subspace.

Both Q-P partitioning strategies share two principal deficiencies. First, any inter-atomic correlation is neglected in the initial state. Such effects are described by two-site ISs, which are either included in the \mathcal{P} subspace (if they correspond to accessible final states) or are completely excluded from the calculation. Second, neither of schemes (i) or (ii) is directly applicable to geometrically more complicated polyatomic systems. Already the helium trimer in equilateral geometry poses difficult problems. To remedy these shortcomings, we propose the following generalization of the localization procedure used in scheme (ii) for homonuclear diatomics. Rather than pairing specific 2h1p configurations, it is possible to diagonalize the whole blocks of the ADC Hamiltonian matrix corresponding to all 2h1p configurations defined by the common particle orbital p. The resulting eigenvalues closely reflect the structure of the double-ionization (DI) thresholds of the system—the energies are essentially only uniformly shifted by the presence of an extra electron in the orbital p. The respective eigenstates then represent ISs adapted to the decay problem in hand in such a way that they show the desired one-to-one correspondence with doubly ionized states of the system plus an electron in a virtual orbital or in continuum. Therefore, these adapted ISs can be readily sorted between the \mathcal{P} and Q subspaces on the basis of knowledge of the number of open decay channels.

Fig. 1 illustrates this procedure on the example of helium trimer. It shows eigenvalues E_{2h1p} of the individual Hamiltonian blocks defined by the particle orbital p as functions of its Hartree-Fock energy ε_p . When the particle

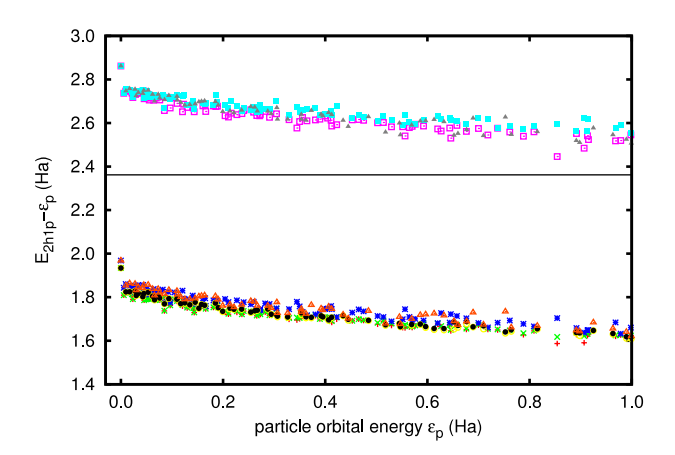


FIG. 1. Eigenvalues of the ADC Hamiltonian sub-blocks corresponding to 2h1p intermediate states with specific particle orbital p characterized by the Hartree-Fock energy ε_p . Solid black line shows the energy E_Φ of the discrete component representing the decaying $({\rm He}_2^+)^*$ – He state. It divides the eigenvalues into the lower-lying group of the six two-site ISs corresponding to open channels (see Table II) and the higher-lying group of ISs contributing to the initial state expansion. The slightly higher lying points at $\epsilon_p=0$ show reference double ionization potentials calculated separately.

orbital energy is subtracted from E_{2h1p} , the eigenvalues are rather independent of ε_p . For each particle orbital p, the resulting eigenvalues sort out into two groups. The lower-energy one corresponds to the six open decay channels listed in Table II, characterized by the two holes being localized on two different atoms. The higher-energy group contains the one-site (with respect to holes localization) states, which are to be included into the initial state expansion. The discrete state energy, marked by the horizontal black line, falls in the large gap between the two groups, separating the open and closed channels.

The most apparent merit of the proposed partitioning scheme is its universality. It can be used for virtually any decay problem which can be described within the ADC(2)x scheme, regardless of the inter- or intra-atomic character of the process. Furthermore, complete space spanned by the ISs is utilized as every adapted IS enters either the initial state or the final state expansions. Namely, ISs of two-site character which do not correspond to energetically open decay channels are included in the Q subspace and provide the description of polarization and inter-atomic correlation in the initial state. The method can be also readily applied to description of decay processes in doubly or multiply ionized systems, provided ADC(2)x scheme for the relevant multi-electron Green's function is available. On the other hand, rigorous analysis of the adapted ISs in the spirit of Ref. 19 is not possible. In fact, experience shows that in rare cases the particle orbital may couple with the two-hole states in such a way that the energy ordering of adapted ISs does not correspond to the DI spectrum. Such problems can however be detected by comparison of the 2h part of the adapted ISs wave functions with those of the decay channels. Generally, the approach works well if there is either pronounced energy gap between open and closed decay channels or if the decay channels show distinct spatial character in terms of hole localization. In the present case, both criteria are met as demonstrated in Fig. 1.

D. Stieltjes imaging

Despite the ability of the ADC(n) scheme to produce 2h1p wave functions χ_i in the continuum region of the spectrum as the eigenfunctions of the Hamiltonian in the \mathcal{P} subspace, the use of \mathcal{L}^2 basis prevents their straightforward use as approximate continuum states in formula (4). The reason is that these wave functions do not satisfy proper scattering boundary conditions and are normalized to unity rather than energy (cf. Eq. (3)),

$$\langle \chi_i | \chi_j \rangle = \delta_{i,j}. \tag{11}$$

Furthermore, the discretized spectrum has to be interpolated in order to satisfy the energy conservation relation for the non-radiative decay process, $E = E_{\Phi}$. These problems can be efficiently solved using the computational technique based on the Stieltjes-Chebyshev moment theory, known as the Stieltjes imaging.²⁵ The approach relies on the fact that while the discretized wave functions χ_i cannot be used to evaluate decay width (4) directly, they provide good approximations of its spectral moments (E_i is the eigenenergy corresponding

to χ_i),

224310-5

$$S_{k} = \sum_{\beta=1}^{N_{c}} \int E^{k} |\langle \Phi | \hat{H} - E | \chi_{\beta, \epsilon_{\beta}} \rangle|^{2} dE$$

$$\approx \sum_{i} (E_{i})^{k} |\langle \Phi | \hat{H} - E_{i} | \chi_{i} \rangle|^{2}.$$
(12)

Here, we have used the assumption that, in the spatial region spanned by the discrete state which contributes to the coupling matrix elements, the solutions χ_i can replace the basis formed by exact continuum wave functions,

$$\sum_{\beta=1}^{N_c} \int |\chi_{\beta,\epsilon_{\beta}}\rangle\langle\chi_{\beta,\epsilon_{\beta}}| \approx \sum_{i} |\chi_{i}\rangle\langle\chi_{i}|.$$
 (13)

The correct value of the decay width can then be recovered using the techniques of moment theory. An efficient realization of the Stieltjes imaging procedure is described in Ref. 29. Convergence of the calculations can be controlled by performing series of consecutive approximations using increasing number of spectral moments S_k .

The incorrect boundary conditions satisfied by the χ_i wave functions also complicate evaluation of partial decay widths. This problem can be solved by constructing suitable channel projectors P_{β} and repeating the Stieltjes imaging procedure with projected continuum functions $P_{\beta}\chi_i$ for each channel. In the present case, the projectors have been constructed using the lowest order expansions of the 2h wave functions of the doubly ionized decay channels.

III. ICD IN HELIUM TRIMER

The calculations of the decay widths in helium trimer were carried out using the MOLCAS quantum chemistry package³⁰ for the Hartree-Fock self-consistent field (SCF) solution and two-electron integral transformation. Our own ADC(2)x code for 1p-GF was utilized. On the atomic centers, cc-pV6Z basis of Dunning et al. 31 was used, augmented by [9s,9p,9d] continuum-like Gaussian functions of Kaufmann-Baumeister-Jungen (KBJ) type. ³² Additional [5s, 5p, 5d] KBJ basis sets were placed on four ghost centers located at bond midpoints and the center of the triangle. This choice ensured both stable and convergent Stieltjes imaging procedures and good convergence of the resulting decay widths in the basis set. Owing to the complexity of the computational procedure, it is very difficult to assess the overall accuracy of the results. Various previous calculations and comparison with data available in the literature suggest a typical error of 10%-20%. 18-20 Good agreement between measured and simulated ICD spectra in helium dimer³ supports the adequacy of the method for the calculation of the decay widths in He clusters.

A. Total interatomic decay widths

The isosceles geometry of the helium trimer and its description used in this paper are shown in Fig. 2. In this configuration, the atoms A and B form a dimer with internuclear distance r and atom C moves along the z axis. Unless specified otherwise, the dimer internuclear distance

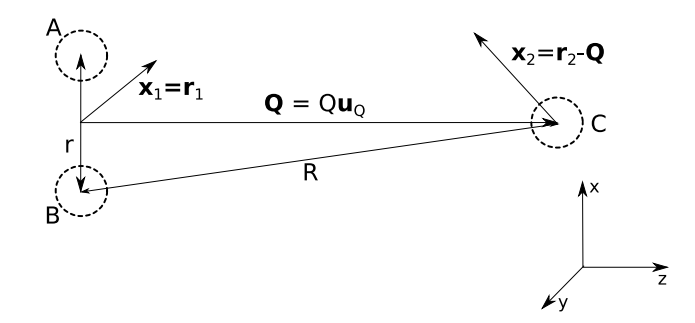


FIG. 2. Geometry of the helium trimer and position vectors used in derivation of the long-range behavior of the partial decay widths. All atoms lie in the $\langle xz \rangle$ plane. In isosceles geometry, the distance between atoms A and B constituting the dimer part is fixed at r=4 Å. Vector \mathbf{x}_1 denotes the position of an electron localized on the dimer AB relative to origin of the coordinate system (center of the dimer), \mathbf{x}_2 is the position of an electron localized on the atom C relative to this atom. \mathbf{Q} is the position vector of the atom C relative to the origin, \mathbf{u}_Q is the unit vector pointing in its direction. R stands for the distance between atom C and individual atoms in the dimer.

is fixed at r = 4 Å in figures through the paper. The mean interatomic distance of 10.4 Å observed in the helium trimer is fairly large from the point of view of interatomic decay transitions and was found to contribute negligibly to the ICD process in the dimer.³ The value of r chosen for the presentation, which corresponds to the maximum in the pair distribution function,² is relevant for the process and also leads to lucid and comprehensible results suitable for the intended discussion.

Table I lists all ionized-excited metastable (ICD-active) states characterized by excitation of an electron into the second atomic shell, which are considered in the present work. For all the states, excitation energy relative to the ground state electronic configuration is 64.3 eV (ADC(2)x method, equilateral geometry with interatomic distance r = R = 4 Å). Second column of Table I shows the notation used to characterize individual states based on their symmetry classification in C_{2v} point group. At large distances Q, the trimer can be described as a dimer AB with MOs $n\sigma_{g,u}$ and $n\pi_{g,u}$ and an individual atom C with atomic orbitals ns and np. Symmetries of the diatomic and atomic fragments are given in parentheses. In the next column, classification in C_s point group is added to mediate the connection to less symmetrical arrangements with the atom C moved away from the z-axis. Fourth column shows leading 2h1p configurations (in terms of the MOs) of the states which is valid for large atom-dimer distance Q. To further facilitate the comprehension of the nature of the individual states, electronic configurations in terms of atomic orbitals (AO) are schematically given in the last column. Information about the spin is omitted for clarity as it is evident from other columns.

The six doubly ionized states (decay channels) of the trimer accessible via ICD are given in Table II in similar notation. At the equilateral geometry with R=4 Å, the respective double ionization energies are 52.4 eV, well below the energy of the initial states given above. With increasing interatomic distance, this energy further decreases as a result of reduced Coulomb repulsion between the positive charges distributed among two atoms. The energy of the initial state,

TABLE I. Designations in C_{2v} and C_s groups and leading asymptotic molecular orbital (MO) occupations (relative to the ground state of He₃) of metastable ionized-excited states characterized by excitation to second shell. In the last column, electronic configuration is given in terms of atomic orbitals (AO).

	C_{2v}	C_s	MO occupation (rel. to ground state)	AO occupation
1	$^2A_1(^1\Sigma_g^+/^2S)$	$^2A'$	$1s^{-2}2s^1$	$1s_A^2 1s_B^2 2s_C^1$
2	${}^{2}A_{1}({}^{2}\Sigma_{g}^{+}/{}^{1}S)$	$^2A'$	$^{1}(1\sigma_{g}^{-2}+1\sigma_{u}^{-2})2\sigma_{g}^{1} \& ^{1}(1\sigma_{g}^{-1}1\sigma_{u}^{-1})2\sigma_{u}^{1}$	$2s_A^1 1s_B^2 1s_C^2 + (A \rightleftharpoons B)$
3	$^2B_1(^2\Sigma_u^+/^1S)$	$^2A'$	$^{1}(1\sigma_{g}^{-2}+1\sigma_{u}^{-2})2\sigma_{u}^{1} \& ^{1}(1\sigma_{g}^{-1}1\sigma_{u}^{-1})2\sigma_{g}^{1}$	$2s_A^1 1s_B^2 1s_C^2 - (A \rightleftharpoons B)$
4	$^{2}B_{1}(^{1}\Sigma_{g}^{+}/^{2}P_{x})$	$^2A'$	$1s^{-2}2p_x^1$	$1s_A^2 1s_B^2 2p_{x,C}^1$
5	$^{2}B_{2}(^{1}\Sigma_{g}^{+}/^{2}P_{y})$	$^2A''$	$1s^{-2}2p_{y}^{1}$	$1s_A^2 1s_B^2 2p_{y,C}^1$
6	$^2A_1(^1\Sigma_g^+/^2P_z)$	$^2A'$	$1s^{-2}2p_{z}^{1}$	$1s_A^2 1s_B^2 2p_{z,C}^{1}$
7	$^{2}A_{1}(^{2}\Sigma_{g}^{+}/^{1}S)$	$^2A'$	$^{1}(1\sigma_{g}^{-2}+1\sigma_{u}^{-2})3\sigma_{g}^{1}$ & $^{1}(1\sigma_{g}^{-1}1\sigma_{u}^{-1})3\sigma_{u}^{1}$	$2p_{x,A}^{1} 1s_{B}^{2} 1s_{C}^{2} + (A \rightleftharpoons B)$
8	${}^{2}B_{1}({}^{2}\Sigma_{u}^{+}/{}^{1}S)$	$^2A'$	$^{1}(1\sigma_{g}^{-2}+1\sigma_{u}^{-2})3\sigma_{u}^{1} \& ^{1}(1\sigma_{g}^{-1}1\sigma_{u}^{-1})3\sigma_{g}^{1}$	$2p_{x,A}^{1} 1s_{B}^{2} 1s_{C}^{2} - (A \rightleftharpoons B)$
9	$^{2}A_{2}(^{2}\Pi_{g}/^{1}S)$	$^2A''$	$^{1}(1\sigma_{g}^{-2}+1\sigma_{u}^{-2})1\pi_{yg}^{1} \& ^{1}(1\sigma_{g}^{-1}1\sigma_{u}^{-1})1\pi_{yu}^{1}$	$2p_{y,A}^{1} 1s_{B}^{2} 1s_{C}^{2} + (A \rightleftharpoons B)$
10	$^{2}B_{2}(^{2}\Pi_{u}/^{1}S)$	$^2A''$	$^{1}(1\sigma_{g}^{-2}+1\sigma_{u}^{-2})1\pi_{yu}^{1} \& ^{1}(1\sigma_{g}^{-1}1\sigma_{u}^{-1})1\pi_{yg}^{1}$	$2p_{y,A}^{1} 1s_B^2 1s_C^2 - (A \rightleftharpoons B)$
11	$^{2}B_{1}(^{2}\Pi_{g}/^{1}S)$	$^2A'$	$^{1}(1\sigma_{g}^{-2}+1\sigma_{u}^{-2})1\pi_{zg}^{1} \& ^{1}(1\sigma_{g}^{-1}1\sigma_{u}^{-1})1\pi_{zu}^{1}$	$2p_{z,A}^{1} 1s_{B}^{2} 1s_{C}^{2} + (A \rightleftharpoons B)$
12	$^2A_1(^2\Pi_u/^1S)$	$^2A'$	$^{1}(1\sigma_{g}^{-2}+1\sigma_{u}^{-2})1\pi_{zu}^{1}$ & $^{1}(1\sigma_{g}^{-1}1\sigma_{u}^{-1})1\pi_{zg}^{1}$	$2p_{z,A}^{1} 1s_B^2 1s_C^2 - (A \rightleftharpoons B)$

on the other hand, is almost independent of the geometry due to the one-site character of the excitation.

In Table I, the metastable states are divided into three groups. The first group of states 1-3 is characterized by an excitation into the 2σ and 2s orbitals. The corresponding total ICD decay widths are shown in Fig. 3. ICD from this group of states is distinguished by the fact that the local $2s \rightarrow 1s$ de-excitation transition is forbidden at all orders of multipole expansion.⁶ As a result, the respective decay widths are determined by spatial orbital overlap between the atoms and show an exponential decrease with the distance Q. Close past the equilateral geometry, the dimer- or atom-localized character of the excitation is revealed. For states 2 and 3, the decay widths stabilize at the values corresponding to a dimer with fixed interatomic distance of r = 4 Å since the distant third atom does not significantly influence the decay any more. On the other hand, state 1 with the excitation localized on the individual atom can only decay via interaction with the dimer and the width continues to decrease exponentially even beyond this point. In the present paper, we do not discuss these states further and focus only on the remaining nine metastable states.

The total decay widths for the metastable states characterized by excitation of an electron into the 2p atomic shell (i.e., into 2p on the atom C and 1π or 3σ on the dimer AB) are shown in Fig. 4. We again observe two qualitatively different groups. States 4–6 are of He₂ – (He⁺)* character and the respective decay widths decrease with Q

for all geometries. For larger Q, the widths depend on the interatomic distance as Q^{-6} , which is typical for ICD dominated by dipole-allowed electronic transitions.³³ Apart from very small atom-dimer distances, the fastest decaying is state 6 with occupied $2p_z$ orbital, oriented towards the dimer. The decay width of state 4 with occupied $2p_x$ orbital (oriented parallel to the dimer axis), which decays most efficiently at shortest distances, asymptotically approaches the slowest state of $2p_y$ character (perpendicular to the trimer plane). These findings are in complete agreement with the previous analysis of asymptotic formulae for ICD widths,³⁴ which shows that at large internuclear separations the decay widths are proportional to the interaction energy between two classical dipoles with appropriately aligned dipole moments.

In Fig. 5, the three decay widths are plotted against the interatomic distance R and compared to the case of sole helium dimer. The dimer decay widths were computed using the same method and equivalent basis set as for the trimer and averaged over gerade and ungerade parity of the decaying states. That is, $\Gamma_{\parallel} = \Gamma_{\Sigma_g^+} + \Gamma_{\Sigma_u^+}$ and $\Gamma_{\perp} = \Gamma_{\Pi_g} + \Gamma_{\Pi_u}$ are shown as representative doubled dimer widths of states with electron excited into the 2p orbitals oriented along and parallel to the dimer axis, respectively. The simplest comparison is obtained for the trimer state with the $2p_y$ excitation, which is of purely perpendicular character with respect to C-A/B bonds and its decay width follows Γ_{\perp} almost precisely for all distances. The other two states with $2p_z$ and $2p_x$ excitations change their character from parallel to perpendicular and vice versa

TABLE II. C_{2v} and C_s designations and asymptotic MO occupations (relative to the ground state of He₃) of doubly ionized channels accessible via ICD from the metastable states given in Table I. In the last column, electronic configuration is given in terms of atomic orbitals (AO).

	C_{2v}	C_s	MO occupation (rel. to ground state)	AO occupation
1	$^{3}A_{1}(^{2}\Sigma_{g}^{+}/^{2}S)$	³ A'	$^{3}(1\sigma_{g}^{-1}1s^{-1})$	$1s_A^1 1s_B^2 1s_C^1 + (A \leftrightharpoons B)$
2	${}^{1}A_{1}({}^{2}\Sigma_{g}^{+}/{}^{2}S)$	$^{1}A'$	$(1\sigma_{g}^{-1}1s^{-1})$	$1s_A^{1} 1s_B^{2} 1s_C^{1} + (A \leftrightharpoons B)$
3	${}^{1}A_{1}({}^{1}\Sigma_{g}^{+}/{}^{1}S)$	$^{1}A'$	$(1\sigma_{g}^{-2}-1\sigma_{u}^{-2})$	$1s_A^1 1s_B^1 1s_C^2$
4	${}^{3}B_{1}({}^{2}\Sigma_{u}^{+}/{}^{2}S)$	$^3A'$	$3(1\sigma_u^{-1}1s^{-1})$	$1s_A^1 1s_B^2 1s_C^1 - (A \leftrightharpoons B)$
5	${}^{1}B_{1}({}^{2}\Sigma_{u}^{+}/{}^{2}S)$	$^{1}A'$	$(1\sigma_u^{-1}1s^{-1})$	$1s_A^{1} 1s_B^{2} 1s_C^{1} - (A \leftrightharpoons B)$
6	$^3B_1(^3\Sigma_g^+/^1S)$	$^3A'$	$^{3}(1\sigma_{g}^{-1}1\sigma_{u}^{-1})$	$1s_A^1 1s_B^1 1s_C^2$

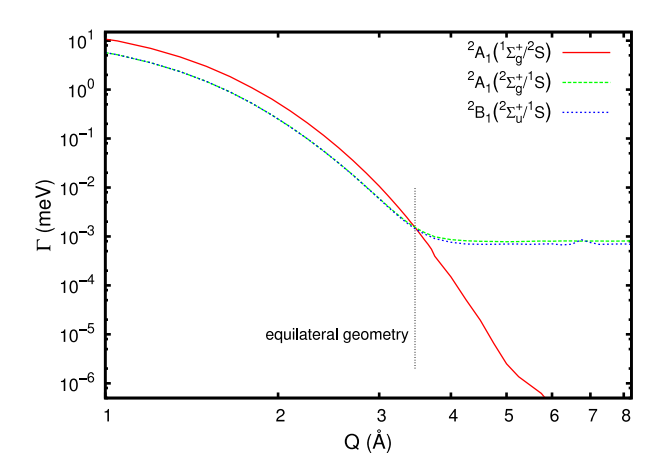


FIG. 3. Total decay widths of the metastable states with an electron excited into 2s or 2σ virtual orbital (states 1–3 in Table I).

going from large to small interatomic distances. At very small distances, the decay width of the $2p_x$ -like state rises above $2\Gamma_{\Sigma_g^+}$, which is the largest width found in the dimer,⁶ even though the state is not of purely parallel character. This shows that mutual interaction between the neighboring atoms can enhance the efficiency of the decay process. The width of the $2p_z$ -like state, on the other hand, falls below the average Γ_{\perp} but still stays above $2\Gamma_{\Pi_u}$ (the smallest dimer width).

The remaining six states shown in Fig. 4 correspond to the initial ionization and excitation being localized on the dimer as $(\text{He}_2^+)^*$ – He. The respective decay widths first decrease with the dimer-atom distance Q. Around Q=6 Å, the decay becomes dominated by local dimer transitions and the decay widths stabilize at the characteristic dimer values corresponding to r=4 Å. In accordance with the helium dimer results⁶ and general conclusions drawn in Ref. 34, ${}^2A_1({}^2\Sigma_g^+/{}^1S)$ and ${}^2B_1({}^2\Sigma_u^+/{}^1S)$ states are the fastest decaying in this group. In the atomic nomenclature, 2p orbitals oriented along the dimer axis are occupied in these states. The other four states with 2p orbitals oriented perpendicular to the dimer axis show decay widths of similar magnitudes. Only around equilateral geometry, the decay of the pair of states 11 and $12 \, [{}^2B_1({}^2\Pi_g/{}^1S), {}^2A_1({}^2\Pi_u/{}^1S)]$ is enhanced, which can

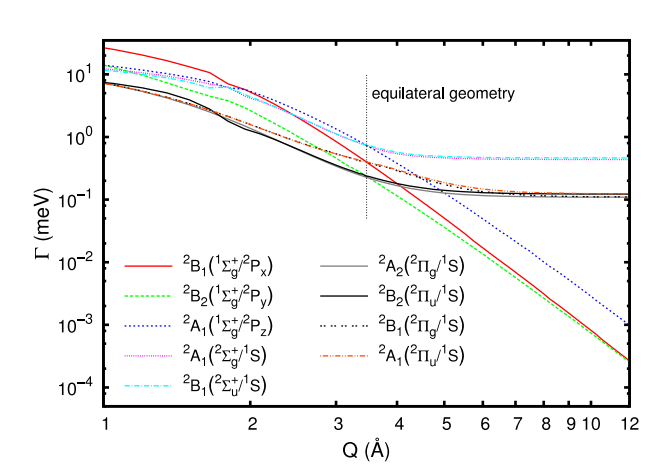


FIG. 4. Total decay widths of the metastable states with an electron excited into 2p, 1π , or 3σ virtual orbital.

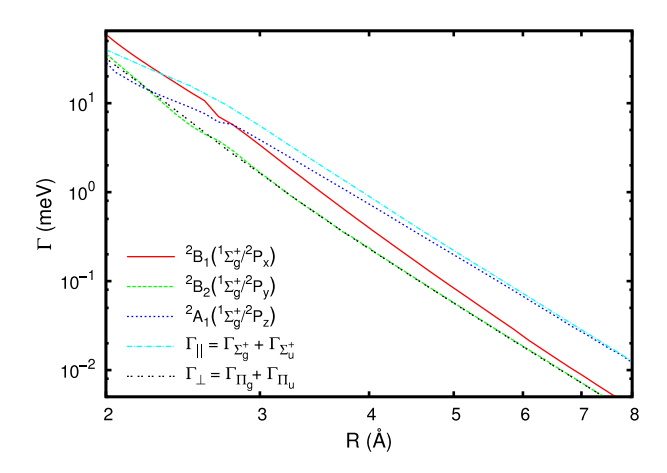


FIG. 5. Comparison of the total decay widths of the states with excitation localized on the atom C with the ICD decay widths in a sole helium dimer. For the dimer, twice the averages over the parity of metastable states is plotted for the Σ and Π symmetries.

be explained by the orientation of the occupied 2p orbitals towards the atom C.

Dependence of the total decay widths on the interatomic distance R in equilateral geometry (r = R) for the same nine metastable states is shown in Fig. 6. In this configuration, all decay widths decrease uniformly according to the R^{-6} rule. More interestingly, with the exception of very compact arrangements all the nine states fall into three groups. The ratios of the respective decay widths are 1:1.76:3.25. The most slowly decaying group is characterized by excitation of an electron into the p_u atomic-like orbital, which is perpendicular to the trimer plane. To clearly describe the other two groups encompassing excitations into p orbitals in the plane is more difficult. However, examining the relevant MOs dominantly contributing to the individual states, the fastest decaying group can be roughly characterized by atomic-like p-orbitals lying along the axes of the angles of the triangle while the middle group by p-orbitals perpendicular to these axes. Making use of the aforementioned relationship between the ICD decay width and the interaction energy between two classical dipoles,³⁴ this picture predicts the ratios to be 1:1.56:3.06 in good agreement with the ab initio results.

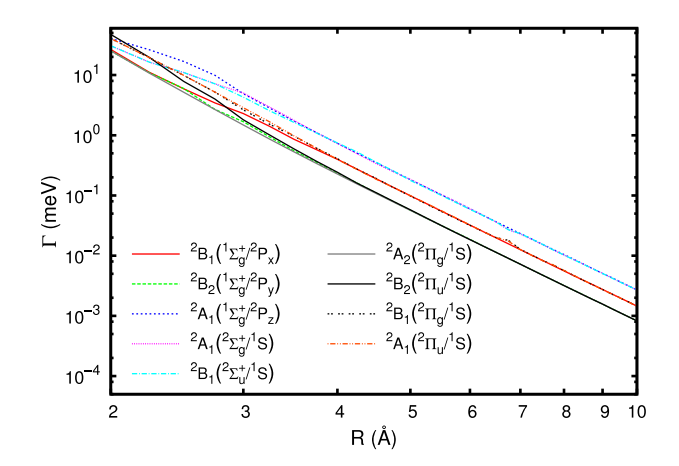


FIG. 6. Total decay widths of the metastable states with an electron excited into 2p atomic-like orbitals (same states as in Fig. 4) in equilateral geometry of the trimer.

B. Partial decay widths and the three-electron ETMD

In this subsection, we investigate partial decay widths for individual relaxation transitions, focusing again mainly on the isosceles geometry of the trimer. Fig. 7 shows the partial decay widths for the ${}^2A_1({}^1\Sigma_g^+/{}^2P_z)$ state of the ${\rm He_2}-({\rm He}^+)^*$ character. For the ${\rm He_2}^+-{\rm He}^+$ channels, their dependence on the distance Q complies with the behavior expected based on the study of ICD in He dimer. They decrease for all distances almost exactly as R^{-6} , manifesting the dipole-dipole character of the interaction. Note that despite the doubly logarithmic scale, in the $\Gamma(Q)$ plot this dependence does not correspond to a straight line since $R=\sqrt{Q^2+r^2/4}$. The triplet channels are stronger while the parity of the empty 1σ dimer orbital does not play any significant role (except for very small distances).

The partial widths corresponding to the remaining two channels of He_2^{2+} – He character drop very quickly with increasing atom-dimer distance as they can be populated exclusively by a process similar to ETMD, ¹⁷ which is efficient only in regions with significant spatial overlap between the orbitals of the dimer and the solitary atom C. Such transitions are characteristic by an exponential decrease of the respective partial decay widths with the interatomic distance. In the present case, the ETMD-like relaxation pathway belongs to the ETMD(3) class (in the final state, the two vacancies are distributed over both atoms of the dimer) and involves three electrons: as in the ETMD(3) process described in the Introduction, a neighboring atom donates an electron to fill the initial vacancy on the ion and the released energy is transferred to another neighbor, ejecting the secondary electron. Additionally, in order to reach the He_2^{2+} – He final state in which the atom C is left in its ground electronic configuration, the electron initially excited into the 2p orbital has to drop back into the 1s orbital.

As can be expected for a process which is forbidden at the lowest order of perturbation theory, the respective partial decay widths are at least two orders of magnitude smaller than those corresponding to the ICD channels. Furthermore, it should be pointed out that below the equilateral geometry, the MOs are

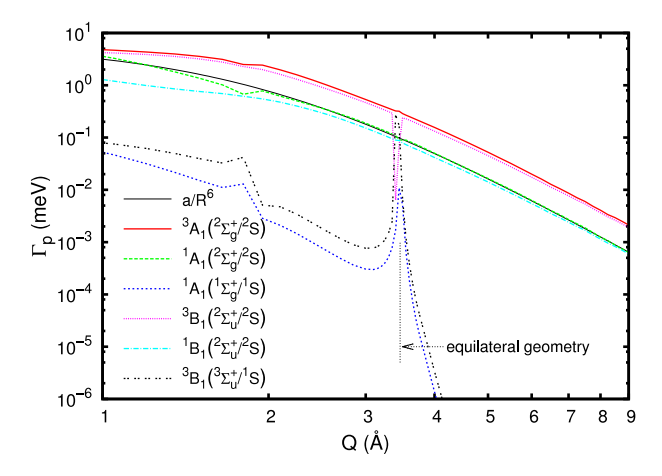


FIG. 7. Partial decay widths for the ${}^2A_1({}^1\Sigma_g^+/{}^2P_z)$ decaying state. The solid thin black line shows the fit of the R^{-6} asymptotic dependence to the ${}^1A_1({}^2\Sigma_g^+/{}^2S)$ partial width. Note that despite the doubly logarithmic scale it is not a straight line as $R = \sqrt{O^2 + r^2/4}$.

strongly delocalized over both the dimer and the solitary atom and, therefore, the distinction between ICD and three-electron ETMD channels is not sharp. The values of the corresponding partial widths below Q=3 Å, which are comparable to the typical two-electron ETMD decay widths (0.09 meV at the equilibrium geometry of NeKr₂¹⁷), are to be attributed to this mixing. The sharp peaks in the ETMD-like and certain ICD partial widths near equilateral geometry have the same origin as the mixing is enhanced due to avoided crossings between the respective decay channels. Only beyond this geometry the character of the channels clarifies, which is manifested by the rapid drop of the ETMD partial widths.

Fig. 8 shows partial decay widths for the ${}^2B_1({}^2\Pi_e/{}^1S)$ state of $(He_2^+)^*$ – He, in which the $1\pi_z$ orbital (oriented in the trimer plane towards the atom C) is occupied in the excited dimer. We observe that the decay channels sort out into three qualitatively distinct pairs. First, the local dimer He_2^{2+} – He channels show partial widths which are constant beyond equilateral geometry since the dimer internuclear distance r is fixed. However, only two of the remaining four partial widths corresponding to $He_2^+ - He^+$ channels decrease according to the R^{-6} dipoledipole rule. The $A_1(^2\Sigma_g^+/^2S)$ channels, in which the empty 1σ orbital has the same parity as the initial state of the dimer, show partial widths decreasing as R^{-8} . We elaborate in Section III C that this is a consequence of dipole-forbidden relaxation transition within the dimer. The ${}^2A_1({}^2\Pi_u/{}^1S)$ decaying state of the opposite dimer parity exhibits the same picture, only the dipole-allowed and dipole-forbidden characters of the He₂⁺ - He⁺ channels are interchanged. Similar results are obtained also for the ${}^2A_1({}^2\Sigma_u^+/{}^1S)$ and ${}^2B_1({}^2\Sigma_u^+/{}^1S)$ states in which the 3σ orbitals are occupied.

Distinctly different behavior can be observed for the ${}^2A_2({}^2\Pi_g/{}^1S)$ and ${}^2B_2({}^2\Pi_u/{}^1S)$ decaying states in which one electron is excited into the $1\pi_y$ orbital of the dimer, perpendicular to the trimer plane. Partial widths for the 2A_2 state are shown in Fig. 9. Again, the partial widths corresponding to channels localized on dimer converge to constant values while those corresponding to the $He_2^+ - He^+$ channels of the opposite (ungerade) dimer parity than the initial state decrease as R^{-6} . Partial widths of the $He_2^+ - He^+$ channels

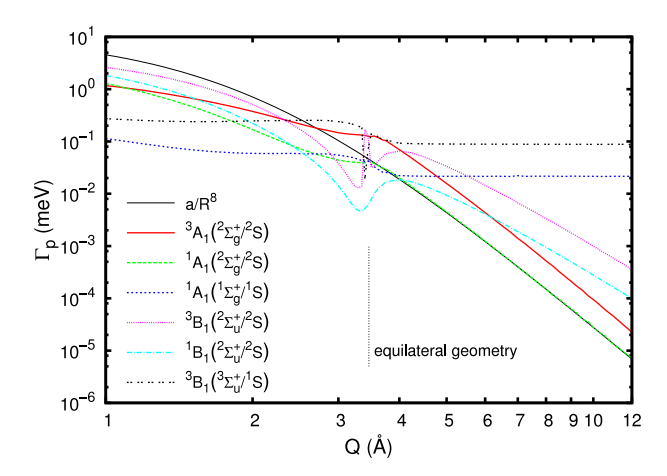


FIG. 8. Partial decay widths for the ${}^2B_1({}^2\Pi_g/{}^1S)$ decaying state. The solid thin black line shows the fit of the R^{-8} asymptotic dependence to the ${}^1A_1({}^2\Sigma_g^+/{}^2S)$ partial width.

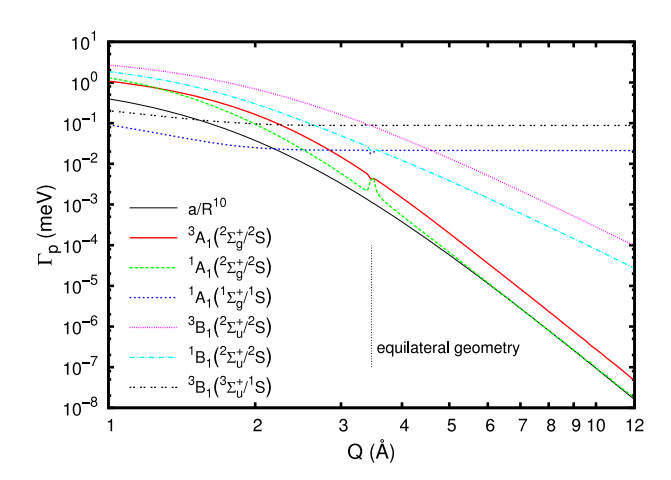


FIG. 9. Partial decay widths for the ${}^2A_2({}^2\Pi_g/{}^1S)$ decaying state. The solid thin black line shows the fit of the R^{-10} asymptotic dependence to the ${}^1A_1({}^2\Sigma_p^+/{}^2S)$ partial width.

of the same dimer parity as the initial state, however, decrease asymptotically as fast as R^{-10} . Since the de-excitation transition on the dimer is equivalent to the cases discussed in the previous paragraph, it is clear that selection rules on the

ionization site (atom C) come into play here. In Subsection III C, we provide a detailed analysis of the asymptotic formulae for the partial decay widths in the spirit of the derivation of the dipole-dipole rule performed in Ref. 33 in order to elucidate the underlying mechanism.

C. Asymptotic dependence of the partial decay widths on dimer-atom distance

The geometry and position vectors used in the following derivation are shown in Fig. 2. In this section, we derive the asymptotic formulae for some of the partial decay widths in terms of inverse dimer-atom distance 1/Q. Note that in the figures we compare the *ab initio* data with asymptotic trends in terms of inverse atom-atom distance 1/R. The reason for this inconsistency is that the derivation is considerably simpler and more transparent for 1/Q. The distance R is, however, more physical and the R^{-n} trends are manifested in the calculated *ab initio* partial widths already for smaller atom-dimer distances. Asymptotically, the difference is insignificant.

In the notation of Fig. 2, the Coulomb operator in atomic units can be expanded in terms of 1/Q as

$$\frac{1}{|\mathbf{r}_{1} - \mathbf{r}_{2}|} = \frac{1}{Q} + \frac{\mathbf{u}_{Q}.(\mathbf{x}_{1} - \mathbf{x}_{2})}{Q^{2}} + \frac{3(\mathbf{u}_{Q}.(\mathbf{x}_{1} - \mathbf{x}_{2}))^{2} - (\mathbf{x}_{1} - \mathbf{x}_{2})^{2}}{2Q^{3}} + \frac{\mathbf{u}_{Q}.(\mathbf{x}_{1} - \mathbf{x}_{2})\left[3(\mathbf{u}_{Q}.(\mathbf{x}_{1} - \mathbf{x}_{2}))^{2} - 9(\mathbf{x}_{1} - \mathbf{x}_{2})^{2}\right]}{6Q^{4}} + \frac{3(\mathbf{x}_{1} - \mathbf{x}_{2})^{4} - 15(\mathbf{u}_{Q}.(\mathbf{x}_{1} - \mathbf{x}_{2}))^{2}(\mathbf{x}_{1} - \mathbf{x}_{2})^{2} + 35(\mathbf{u}_{Q}.(\mathbf{x}_{1} - \mathbf{x}_{2}))^{4}}{8Q^{5}} + O\left(\frac{1}{Q^{6}}\right).$$
(14)

In our particular case, the expression can be further significantly simplified using the specific form of the unit vector $\mathbf{u}_Q = (0,0,1)$. For the explicit evaluation of the required coupling elements, we use the spin-free working equations for 1p-GF/ADC(2)x derived from Eq. (A12) in Ref. 28.

Let us first investigate the decay of the ${}^2B_1({}^2\Pi_g/{}^1S)$ state into the ${}^1A_1({}^2\Sigma_g^+/{}^2S)$ channel, which shows the R^{-8} asymptotic behavior (cf. Fig. 8). According to Ref. 19 and Table I, the one-site (He $_2^+$)* – He state of this symmetry can be described as a linear combination of two leading 2h1p configurations, ${}^1(1\sigma_g^{-2}+1\sigma_u^{-2})1\pi_{zg}^1$ and ${}^1(1\sigma_g^{-1}1\sigma_u^{-1})1\pi_{zu}^1$. The final state is represented by a single configuration ${}^1(1\sigma_g^{-1}1s^{-1})k^1$, where k stands for the single-particle continuum wave function describing the outgoing electron, centered on the solitary atom C. The coupling matrix elements relevant for the evaluation of decay width (4) then read

$$\langle {}^{1}(1\sigma_{g} 1\sigma_{g}) 1\pi_{zg} |\hat{H}|^{1}(1\sigma_{g} 1s) k \rangle$$

$$= \frac{1}{2}(1\pi_{zg} 1\sigma_{g} |k 1s) - (1\pi_{zg} 1s |k 1\sigma_{g})$$
 (15)

and

$$\langle {}^{1}(1\sigma_{g} 1\sigma_{u}) 1\pi_{zu} | \hat{H} | {}^{1}(1\sigma_{g} 1s) k \rangle$$

$$= \frac{1}{2} (1\pi_{zu} 1\sigma_{u} | k 1s) - (1\pi_{zu} 1s | k 1\sigma_{u})$$
 (16)

for the first and second 2h1p configuration contributing to the initial state, respectively. Here, we have employed the notation for two-electron integrals over spatial orbitals

$$(ij|kl) = \int \psi_i^*(\mathbf{r}_1)\psi_j(\mathbf{r}_1) \frac{1}{|\mathbf{r}_1 - \mathbf{r}_2|} \psi_k^*(\mathbf{r}_2)\psi_l(\mathbf{r}_2) d\mathbf{r}_1 d\mathbf{r}_2.$$
 (17)

Note that for the ${}^{1}(1\sigma_{u} \, 1\sigma_{u}) \, 1\pi_{zg}$ component of the first configuration, the matrix element vanishes identically due to the opposite parity of the final $1\sigma_{g}$ and both initial $1\sigma_{u}$ vacancies.

For large Q, only the first terms on the right hand sides of Eqs. (15) and (16) survive. The other terms correspond to electron exchange pathways, which are nonzero only in the spatial regions where the dimer and atomic electronic wave functions overlap. Furthermore, considering the symmetries of the involved orbitals in terms of the C_{2v} point group, the continuum wave functions k must in both cases have the B_1 symmetry, which corresponds to p-wave polarized along the x-axis. Therefore, using expansion (14) of the Coulomb operator, the first non-vanishing contributions to the coupling matrix elements are found to be

$$\langle {}^{1}(1\sigma_{g} 1\sigma_{g}) 1\pi_{zg} | \hat{H} | {}^{1}(1\sigma_{g} 1s) k \rangle$$

$$\approx \frac{3}{2Q^{4}} \langle 1\pi_{zg} | x_{1}z_{1} | 1\sigma_{g} \rangle \langle k_{px} | x_{2} | 1s \rangle + O\left(\frac{1}{Q^{5}}\right)$$
(18)

and

$$\langle {}^{1}(1\sigma_{g} 1\sigma_{u}) 1\pi_{zu} | \hat{H} | {}^{1}(1\sigma_{g} 1s) k \rangle$$

$$\approx \frac{3}{2O^{4}} \langle 1\pi_{zu} | x_{1}z_{1} | 1\sigma_{u} \rangle \langle k_{p_{x}} | x_{2} | 1s \rangle + O\left(\frac{1}{O^{5}}\right). \tag{19}$$

The 1π and 1σ dimer orbitals of the same parity can only be coupled by a quadrupole operator, resulting in a Q^{-4} leading dependence of the coupling elements and thus Q^{-8} of the partial decay width, in agreement with the *ab initio* results shown in Fig. 8. Similar quadrupole-dipole character of ICD was previously studied in the case of $ns \rightarrow (n-1)d$ transitions in the elements of the periodic table groups $3-12.^{35}$ Obviously, if the parity of the 1σ orbitals is switched in Eqs. (18) and (19), the dipole operator would be sufficient to couple them with the respective $1\pi_z$ orbitals, resulting in the Q^{-3} dependence of the coupling element as observed for the $1\sigma = 1$ dependence of the coupling element as observed for the $1\sigma = 1$ dependence of the coupling element as observed for the $1\sigma = 1$ dependence of the coupling element as observed for the $1\sigma = 1$ dependence of the coupling element as observed for the $1\sigma = 1$ dependence of the coupling element as observed for the $1\sigma = 1$ dependence of the coupling element as observed for the $1\sigma = 1$ dependence of the coupling element as observed for the $1\sigma = 1$ dependence of the coupling element as observed for the $1\sigma = 1$ dependence of the coupling element as observed for the $1\sigma = 1$ dependence of the coupling element as observed for the $1\sigma = 1$ dependence of the coupling element as observed for the $1\sigma = 1$ dependence of the coupling element as observed for the $1\sigma = 1$ dependence of the coupling element as $1\sigma = 1$ dependence of the $1\sigma = 1$ dependence of the coupling element as $1\sigma = 1$ dependence of $1\sigma =$

Let us now turn our attention to the ${}^2A_2({}^2\Pi_g/{}^1S)$ decaying state, for which the partial decay width for the ${}^1A_1({}^2\Sigma_g^+/{}^2S)$ channel decreases as R^{-10} as shown in Fig. 9. The initial state can again be represented as a linear combination of two 2h1p configurations, ${}^1(1\sigma_g^{-2}+1\sigma_u^{-2})1\pi_{yg}^1$ and ${}^1(1\sigma_g^{-1}1\sigma_u^{-1})1\pi_{yu}^1$. The initial-final states coupling matrix elements for large O reads

$$\langle {}^{1}(1\sigma_{g} 1\sigma_{g}) 1\pi_{yg} | \hat{H} | {}^{1}(1\sigma_{g} 1s) k \rangle = \frac{1}{2} (1\pi_{yg} 1\sigma_{g} | k 1s)$$
 (20)

and

$$\langle {}^{1}(1\sigma_{g} 1\sigma_{u}) 1\pi_{yu} | \hat{H} | {}^{1}(1\sigma_{g} 1s) k \rangle = \frac{1}{2}(1\pi_{yu} 1\sigma_{u} | k 1s). \quad (21)$$

In both cases, the two-electron integrals are nonzero only if the continuum wave function k of the electron outgoing from the atomic site C has the A_2 symmetry, which can be satisfied only by d or higher partial wave. In turn, at least quadrupole operator is required to mediate the $1s \rightarrow k$ transition on the atom C and the first non-vanishing contributions to the coupling elements are found in the Q^{-5} term of expansion (14)

$$\langle {}^{1}(1\sigma_{g} 1\sigma_{g}) 1\pi_{yg} | \hat{H} | {}^{1}(1\sigma_{g} 1s) k \rangle$$

$$\approx \frac{3}{2Q^{5}} \langle 1\pi_{yg} | x_{1}y_{1} | 1\sigma_{g} \rangle \langle k_{d_{xy}} | x_{2}y_{2} | 1s \rangle + O\left(\frac{1}{Q^{6}}\right)$$
 (22)

anc

$$\langle {}^{1}(1\sigma_{g} 1\sigma_{u}) 1\pi_{yu} | \hat{H} | {}^{1}(1\sigma_{g} 1s) k \rangle$$

$$\approx \frac{3}{2Q^{5}} \langle 1\pi_{yu} | x_{1}y_{1} | \sigma_{u} \rangle \langle k_{dxy} | x_{2}y_{2} | 1s \rangle + O\left(\frac{1}{Q^{6}}\right). \tag{23}$$

If the parity of the 1σ vacancy in the final state is changed for this particular initial state, not only the relaxation transition on the dimer becomes dipole-allowed, but also the *p*-wave polarized along *y*-axis becomes available for the outgoing electron, which is demonstrated by the R^{-6} dipole-dipole character of the partial widths for the $^{1,3}B_1(^2\Sigma_u^+/^2S)$ final states in Fig. 9. In the analysis of the decay of (n-1)d vacancies in BaZn dimer in Ref. 35, quadrupole-quadrupole character of the ICD transition was identified in the decay of states with magnetic quantum number |m|=2 as a consequence of the symmetry of atomic orbitals involved. In the present case, the

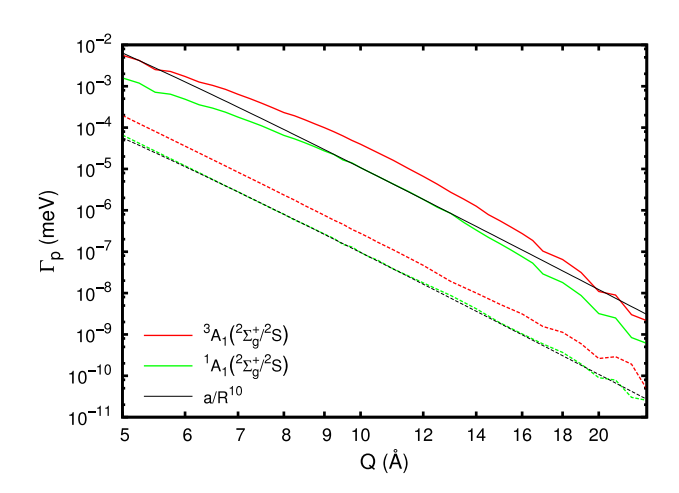


FIG. 10. Partial decay widths for the ${}^2A_2({}^2\Pi_g/{}^1S)$ decaying state for the channels showing the Q^{-10} dependence in symmetrical triangle configuration (dashed lines). Solid lines show the same partial widths for geometry in which the atom C is moved by 0.2 Å from the dimer axis in the xz-plane. Thin black lines show fits of the R^{-10} asymptotic dependence to the ${}^1A_1({}^2\Sigma_g^+/{}^2S)$ partial width for both configurations.

phenomenon originates in the mutual interaction of all three bodies—no equivalent selection rules are found in the helium dimer.⁶

An important question arises whether this effect persists when the reflection symmetry with respect to uz-plane is lifted, i.e., if the atom C is moved away from the z-axis. Fig. 10 shows that the Q^{-10} channels gain significantly more intensity and their decrease is slower at intermediate distances compared to the symmetrical case. For large Q, though, we observe that the respective partial widths tend to decrease even faster than Q^{-10} . It is an indication that they would converge to the symmetrical case widths at asymptotically large distances as the displacement of the atom C becomes insignificant. However, for numerical reasons it is not possible to obtain stable and accurate results for large enough Q to confirm this conjecture. The analysis of less symmetrical geometries is further complicated by the fact that in the C_s point group all the decay channels have the A' symmetry. Since the decay channels are only defined asymptotically with respect to the outgoing electron, true continuum functions are necessary for proper partial widths evaluation. Within the \mathcal{L}^2 basis, we cannot rule out unwanted mixing of the decay channels in the approximative channel projectors employed, since the influence of the outgoing electron being still near is inevitably included. It is therefore difficult to distinguish whether the higher intensity at short distances and subsequent faster decrease of the considered widths is entirely physical or whether it is partly a manifestation of the aforementioned false mixing of decay channels.

IV. CONCLUSIONS

In the present paper, we review the *ab initio* Fano-ADC-Stieltjes method for the calculation of electronic decay widths and present an advanced and universal approach to partitioning of the ADC configuration space into the discrete states and continuum subspaces, which significantly extends

the range of applicability and facilitates the practical use of the method. The method is then used to study the interatomic decay widths in helium trimer. We focus mostly on isosceles configurations in which two atoms form a dimer with fixed internuclear distance and the third atom lies on the dimer axis. All relevant (ICD-active) one-site ionized-excited states of the trimer characterized by excitation of an electron into the second shell are discussed.

The results for the total decay widths comply with the expectations that can be drawn from the previous analysis of the helium dimer. For the metastable states with the excitation localized on the individual atom, the dependence of the widths on the atom-dimer distance follows the well established inverse sixth-power law stemming from the dipoledipole character of the interaction. However, besides the four decay channels corresponding to energy transfer-dominated ICD, we have identified also two channels accessible only by previously unreported three-electron ETMD-like process, in which the electron transfer between solitary atom and the dimer is accompanied by simultaneous local recombination of the initially excited electron on the atom and ionization of the secondary electron from the dimer. However, inspection of the respective partial decay widths shows that in helium trimer such a process is at least two orders of magnitude slower than ICD even for the shortest internuclear distances.

The decay widths of the states with dimer-localized excitation are significantly enhanced by the presence of the third atom if it is near but with the atom-dimer distance increasing beyond equilateral geometry they quickly converge to the values corresponding to isolated dimer at given internuclear distance. These values depend on the orientation of the π or σ dimer orbital occupied by the excited electron. Rather unexpected results were obtained for the respective partial decay widths. For different channels and metastable states we observe not only the typical dipole-dipole R^{-6} power law, but also R^{-8} and even R^{-10} dependence on the internuclear distance. The last one is an indication of a relaxation transition induced by quadrupole-quadrupole interaction, which was confirmed by the analysis of the relevant coupling elements for large atom-dimer distances. Unfortunately, limitations of the present ab initio method prevent unambiguous analysis of this effect in less symmetrical configurations.

By elucidating how three-body effects can influence the known relaxation transitions as well as by showing an example of a new type of decay processes available in clusters, our results push forward our understanding of interatomic decay processes in polyatomic systems. Furthermore, they provide also benchmark data for testing various approximative methods, which will be necessary for evaluation of the decay widths in large systems where fully *ab initio* methods are impractical.

ACKNOWLEDGMENTS

This work has been financially supported by the Czech Science Foundation (Project No. GAČR P208/12/0521). N.S. acknowledges financial state aid managed by the Agence Nationale de la Recherche, as part of the programme

Investissements d'avenir under the Reference No. ANR-11-IDEX-0004-02.

- ¹R. E. Grisenti, W. Schöllkopf, J. P. Toennies, G. C. Hegerfeldt, T. Köhler, and M. Stoll, Phys. Rev. Lett. 85, 2284 (2000).
- ²M. Lewerenz, J. Chem. Phys. **106**, 4596 (1997).
- ³N. Sisourat, N. V. Kryzhevoi, P. Kolorenč, S. Scheit, T. Jahnke, and L. S. Cederbaum, Nat. Phys. **6**, 508 (2010).
- ⁴T. Havermeier, T. Jahnke, K. Kreidi, R. Wallauer, S. Voss, M. Schöffler, S. Schössler, L. Foucar, N. Neumann, J. Titze, H. Sann, M. Kühnel, J. Voigtsberger, J. H. Morilla, W. Schöllkopf, H. Schmidt-Böcking, R. E. Grisenti, and R. Dörner, Phys. Rev. Lett. **104**, 133401 (2010).
- ⁵N. Sisourat, N. V. Kryzhevoi, P. Kolorenč, S. Scheit, and L. S. Cederbaum, Phys. Rev. A **82**, 053401 (2010).
- ⁶P. Kolorenč, N. V. Kryzhevoi, N. Sisourat, and L. S. Cederbaum, Phys. Rev. A **82**, 013422 (2010).
- ⁷T. Havermeier, K. Kreidi, R. Wallauer, S. Voss, M. Schöffler, S. Schössler, L. Foucar, N. Neumann, J. Titze, H. Sann, M. Kühnel, J. Voigtsberger, N. Sisourat, W. Schöllkopf, H. Schmidt-Böcking, R. E. Grisenti, R. Dörner, and T. Jahnke, Phys. Rev. A 82, 063405 (2010).
- ⁸P. Burzynski, F. Trinter, J. B. Williams, M. Weller, M. Waitz, M. Pitzer, J. Voigtsberger, C. Schober, G. Kastirke, C. Müller, C. Goihl, F. Wiegandt, R. Wallauer, A. Kalinin, L. P. H. Schmidt, M. Schöffler, G. Schiwietz, N. Sisourat, T. Jahnke, and R. Dörner, Phys. Rev. A **90**, 022515 (2014).
- ⁹L. S. Cederbaum, J. Zobeley, and F. Tarantelli, Phys. Rev. Lett. **79**, 4778 (1997).
- ¹⁰S. Marburger, O. Kugeler, U. Hergenhahn, and T. Möller, Phys. Rev. Lett. 90, 203401 (2003).
- ¹¹T. Jahnke, A. Czasch, M. S. Schöffler, S. Schössler, A. Knapp, M. Käsz, J. Titze, C. Wimmer, K. Kreidi, R. E. Grisenti, A. Staudte, O. Jagutzki, U. Hergenhahn, H. Schmidt-Böcking, and R. Dörner, Phys. Rev. Lett. 93, 163401 (2004).
- ¹²See http://www.pci.uni-heidelberg.de/tc/usr/icd/ICD.refbase.html for the complete list of ICD papers.
- ¹³J. Voigtsberger, S. Zeller, J. Becht, N. Neumann, F. Sturm, H.-K. Kim, M. Waitz, F. Trinter, M. Kunitski, A. Kalinin, J. Wu, W. Schöllkopf, D. Bressanini, A. Czasch, J. B. Williams, K. Ullmann-Pfleger, L. P. H. Schmidt, M. S. Schöffler, R. E. Grisenti, T. Jahnke, and R. Dörner, Nat. Commun. 5, 5765 (2014).
- ¹⁴M. V. Rama Krishna and K. B. Whaley, J. Chem. Phys. **93**, 6738 (1990); P. Barletta and A. Kievsky, Phys. Rev. A **64**, 042514 (2001); D. Blume, C. H. Greene, and B. D. Esry, J. Chem. Phys. **113**, 2145 (2000).
- ¹⁵M. Kunitski, S. Zeller, J. Voigtsberger, A. Kalinin, L. P. H. Schmidt, M. Schöffler, A. Czasch, W. Schöllkopf, R. E. Grisenti, T. Jahnke, D. Blume, and R. Dörner, Science 348, 551 (2015).
- ¹⁶D. Bressanini and G. Morosi, J. Phys. Chem. A **115**, 10880 (2011).
- ¹⁷J. Zobeley, R. Santra, and L. S. Cederbaum, J. Chem. Phys. **115**, 5076 (2001); M. Förstel, M. Mucke, T. Arion, A. M. Bradshaw, and U. Hergenhahn, Phys. Rev. Lett. **106**, 033402 (2011); V. Stumpf, P. Kolorenč, K. Gokhberg, and L. S. Cederbaum, *ibid.* **110**, 258302 (2013).
- ¹⁸V. Averbukh and L. S. Cederbaum, J. Chem. Phys. **123**, 204107 (2005).
- ¹⁹V. Averbukh and L. S. Cederbaum, J. Chem. Phys. **125**, 094107 (2006).
- ²⁰P. Kolorenč, V. Averbukh, K. Gokhberg, and L. S. Cederbaum, J. Chem. Phys. **129**, 244102 (2008); V. Averbukh, P. Demekhin, P. Kolorenč, S. Scheit, S. D. Stoychev, A. I. Kuleff, Y.-C. Chiang, K. Gokhberg, S. Kopelke, N. Sisourat, and L. S. Cederbaum, J. Electron Spectrosc. Relat. Phenom. **183**, 36 (2011).
- ²¹U. Fano, Phys. Rev. **124**, 1866 (1961).
- ²²H. Feshbach, Rev. Mod. Phys. **36**, 1076 (1964).
- ²³W. Domcke, Phys. Rep. **208**, 97 (1991).
- ²⁴J. Schirmer, Phys. Rev. A **43**, 4647 (1991); F. Mertins and J. Schirmer, *ibid*. **53**, 2140 (1996); A. B. Trofimov and J. Schirmer, J. Chem. Phys. **123**, 144115 (2005).
- ²⁵P. W. Langhoff, in *Electron-Molecule and Photon-Molecule Collisions*, edited by T. Rescigno, V. McKoy, and B. Schenider (Plenum, New York, 1979), p. 183; A. U. Hazi, in *Electron-Molecule and Photon-Molecule Collisions*, edited by T. Rescigno, V. McKoy, and B. Schenider (Plenum, New York, 1979), p. 281.
- ²⁶G. Howat, T. Åberg, and O. Goscinski, J. Phys. B: At. Mol. Phys. 11, 1575 (1978).
- ²⁷J. Schirmer, L. S. Cederbaum, and O. Walter, Phys. Rev. A 28, 1237 (1983).

- ²⁸J. Schirmer, A. B. Trofimov, and G. Stelter, J. Chem. Phys. **109**, 4734 (1998).
- ²⁹F. Müller-Plathe and G. H. F. Diercksen, *Phys. Rev. A* **40**, 696 (1989).
- ³⁰F. Aquilante, L. De Vico, N. Ferré, G. Ghigo, P. Malmqvist, P. Neogrády, T. B. Pedersen, M. Pitoňák, M. Reiher, B. O. Roos, L. Serrano-Andrés, M. Urban, V. Veryazov, and R. Lindh, J. Comput. Chem. 31, 224 (2010).
- ³¹T. Van Mourik, A. Wilson, and T. Dunning, Mol. Phys. **96**, 529 (1999).
- ³²K. Kaufmann, W. Baumeister, and M. Jungen, J. Phys. B: At., Mol. Opt. Phys. 22, 2223 (1989).
- ³³R. Santra and L. S. Cederbaum, Phys. Rep. **368**, 1 (2002).
- ³⁴K. Gokhberg, S. Kopelke, N. V. Kryzhevoi, P. Kolorenč, and L. S. Cederbaum, Phys. Rev. A 81, 013417 (2010).
- ³⁵V. Averbukh, I. B. Müller, and L. S. Cederbaum, Phys. Rev. Lett. **93**, 263002 (2004).